

RP-VIO: Robust Plane-based Visual-Inertial Odometry for Dynamic Environments

Karnik Ram, Chaitanya Kharyal, Sudarshan S. Harithas, K. Madhava Krishna

Abstract—Modern visual-inertial navigation systems (VINS) are faced with a critical challenge in real-world deployment: they need to operate reliably and robustly in highly dynamic environments. Current best solutions merely filter dynamic objects as outliers based on the semantics of the object category. Such an approach does not scale as it requires semantic classifiers to encompass all possibly-moving object classes; this is hard to define, let alone deploy. On the other hand, many real-world environments exhibit strong structural regularities in the form of planes such as walls and ground surfaces, which are also crucially static. We present RP-VIO, a monocular visual-inertial odometry system that leverages the simple geometry of these planes for improved robustness and accuracy in challenging dynamic environments. Since existing datasets have a limited number of dynamic elements, we also present a highly-dynamic, photorealistic synthetic dataset for a more effective evaluation of the capabilities of modern VINS systems. We evaluate our approach on this dataset, and three diverse sequences from standard datasets including two real-world dynamic sequences and show a significant improvement in robustness and accuracy over a state-of-the-art monocular visual-inertial odometry system. We also show in simulation an improvement over a simple dynamic-features masking approach. Our code and dataset are publicly available[†].

I. INTRODUCTION

The visual-inertial navigation systems (VINS) of today are cheap, compact, and provide geometry and pose estimates in real-time with centimeter-level accuracy. VINS are increasingly being used in mobile robot navigation, virtual reality, and augmented reality applications [1]–[3]. Cameras and inertial measurement units (IMUs) in VINS complement each other: IMUs resolve the scale factor ambiguity with monocular cameras, while cameras render the unobservable IMU biases and intrinsics observable. Yet, the approach has some limitations. Apart from the additional hardware that needs to be accurately synchronized and calibrated, the system needs to perform sufficient rotation and acceleration motions to keep the gravity and scale observable [4]. For extended operation, VINS require online calibration where degenerate trajectories may render the extrinsics and intrinsics unobservable [5, 6].

Another significant limitation is their performance in visually dynamic environments that have multiple independently moving objects. The fundamental multiview geometry [7] constraints hold only for static points and lead to errors when applied on dynamic points. This problem is especially significant during the initialization phase of monocular

All authors are with the Robotics Research Center at IIIT Hyderabad, India. Correspondence email: karnikram@gmail.com.

[†]Project page: <https://github.com/karnikram/rp-vio>

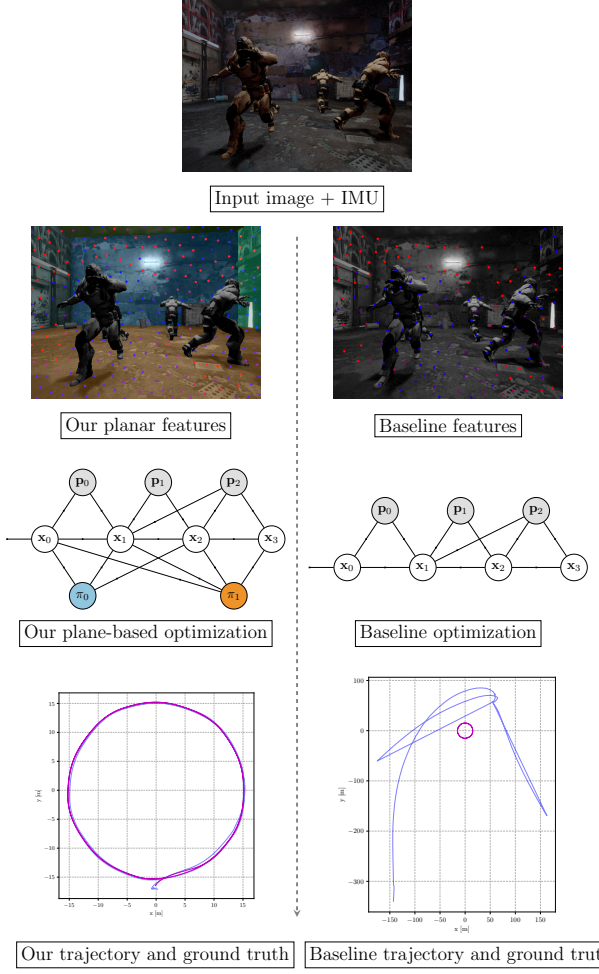


Fig. 1: **Overview**: Motivated by the presence of large planar surfaces in man-made environments, we propose a monocular VIO system that estimates motion only from one or more planes in the scene based on their induced homographies, and ignoring all off-the-plane features. We show that this leads to improved robustness and accuracy in dynamic environments. In the above figure, — (blue) indicates the estimated trajectory and — (magenta) indicates the ground truth.

VINS, where pose estimates from visual SfM are usually directly aligned with the preintegrated IMU measurements to initialize the scale and IMU parameters. Incorrect visual pose estimates at this stage can lead to complete tracking failure, as we demonstrate in our experiments. The traditional approach of applying RANSAC to filter the dynamic features using a fundamental matrix model works well only for a small number of dynamic features, provided the features

are also not following any degenerate motion profiles along the epipolar plane [8]. Motion segmentation approaches to directly predict the motion status of each image pixel often have elaborate multi-stage pipelines to distinguish the egomotion from the object motion, resulting in high computation times [9] that are not yet suitable for real-time SLAM systems.

Current best approaches use semantic labels to filter out features from potentially-dynamic semantic classes [10, 11]. Semantic segmentation, fuelled by deep learning, has seen tremendous progress and can produce accurate semantic labels at frame rate. But the notion of a *dynamic* class is handcrafted, and enumerating all possible dynamic classes leads to intractability. A tractable approach would be to instead directly identify static structures in a scene for feature tracking, bypassing semantics. We note that planar surfaces are the most abundant static regions in everyday man-made environments. Crucially planes also offer a simple geometry that can be further exploited for improved estimation. With this insight, we propose RP-VIO, a plane-based monocular visual-inertial odometry (VIO) system that is tailored for dynamic environments.

RP-VIO uses only features from one or more planes in the scene, identified by a plane segmentation model, and uses the plane-induced homographies for motion estimation. We augment a state-of-the-art monocular VIO system [12] with our proposed homography constraints, and significantly improve performance over the state-of-the-art on an in-house photorealistic synthetic dataset, as well as three diverse sequences from standard datasets including two real-world dynamic sequences.

To summarize, our main contributions are as follows:

- RP-VIO, a monocular VIO system (built atop VINS-Mono [12]) that only uses planar features, and their induced homographies during both initialization and sliding-window estimation for improved robustness and accuracy in dynamic environments.
- A photorealistic visual-inertial dataset, which unlike existing datasets, contains dynamic characters present throughout the sequences (including initialization), and with sufficient IMU excitation.
- An extensive evaluation of our method against [12] on our in-house dataset, an outdoor simulated sequence from the recently released VIODE dataset [10], as well as two challenging real-world sequences from OpenLORIS-Scene [13] and ADVIO [14] using a CNN-based plane segmentation model.

II. RELATED WORK

A. Visual-Inertial Odometry

A concise overview of VINS research can be found in [15]. We focus on closely related visual-inertial odometry algorithms (VIO) herein, which unlike visual-inertial SLAM systems [16, 17], only estimate the trajectory of the device and do not build a globally consistent map.

Filtering-based approaches to VIO still continue to be widely prevalent because of their efficiency. An important

work in this area is the multi-state constraint Kalman filter (MSCKF) [18] which adopts a structureless approach and marginalizes out the landmark positions, avoiding the quadratic EKF cost. A modern, performant implementation can be found in OpenVINS [19].

Optimization-based approaches instead solve for the entire trajectory [20, 21] or a sliding window of recent poses [12, 22], and are generally more accurate and robust. An important enabler for optimization-based VINS is IMU preintegration [23] which allows multiple inertial measurements to be summarized, reducing state space size.

B. Monocular VIO using Planes

Plane-based visual-inertial systems that use stereo or depth sensors have been proposed in many works [21, 24, 25]. In monocular VIO systems however, planes are harder to segment accurately and their depths are also not directly available.

A monocular VIO system that uses only ground plane features, within an UKF was proposed in [26]. They also showed the translation in the direction of the ground-plane normal becomes globally observable, reducing the total number of unobservable directions to three. A direct frame-to-frame planar homography based VIO formulation was proposed in [27] for a downward-facing camera, but assumed a laser rangefinder for accurately estimating the scale. A recent optimization-based monocular VIO system used an efficient plane and line parameterization [28], while also leveraging a deep neural network for plane instance segmentation. However, all of these approaches have only been evaluated in static environments.

C. VIO in Dynamic Environments

A systematic survey of approaches for visual SLAM and visual odometry in dynamic environments can be found in [29]. Broadly, these approaches filter dynamic elements as outliers [10, 11], or jointly estimate the egomotion and the motion of the dynamic elements [30, 31]. Our focus is on the former class of approaches as the latter approaches typically assume device egomotion to be readily estimated.

Relatively fewer approaches have specifically addressed VIO in dynamic environments. A method to detect conflicts between vision-only and inertial-only estimates has been presented in [32], assuming the inertial measurements are always more reliable. [10] exploited semantics to mask out dynamic objects for better egomotion estimation. However, this approach requires an enumeration of static and dynamic classes which is not always possible.

Datasets: The lack of publicly-available visual-inertial datasets that capture the dynamic nature of real-world environments has also made it difficult to evaluate the robustness of existing approaches. Progress has been made on this front with the recent release of the ADVIO [14] and OpenLORIS-Scene [13] datasets. But the sequences in ADVIO are suitable only for a coarse, long-term evaluation of VIO algorithms since their ground truth is only sub-meter accurate. The sequences in OpenLORIS on the other hand were captured

from a ground robot without sufficient excitation for the IMU which leads to unobservability [4], making it difficult to isolate the effect of the dynamic characters. Recently, a challenging simulated dataset was proposed in [10], along with an evaluation of two state-of-the-art VIO algorithms [12, 33] where they showed significant degradation of their accuracy. These sequences however do not contain enough dynamic characters present throughout the sequences, and during the initialization subsequence, which is the most fragile part of the system, there are no dynamic characters at all.

Conclusion: To the best of our knowledge, a monocular VIO system that optimizes over planar homographies and that is targeted at dynamic environments has not been proposed before. A fully dynamic visual-inertial dataset with accurate ground truth, synchronization, and sufficient observability also does not publicly exist.

III. METHOD

While our proposed method is general enough to be integrated into any visual-inertial odometry or SLAM system, in this work we build upon VINS-Mono [12]. VINS-Mono is a state-of-the-art, monocular visual-inertial odometry system that is based on a tightly-coupled sliding-window optimization of preintegrated IMU measurements and visual features. We consider it as a pure VIO system and ignore its relocalization and loop-closure modules. We build upon its front-end to detect and track only planar features in the scene, and introduce the induced planar homography constraints into the initialization and optimization modules.

A. Definitions

W denotes the world frame whose z -axis is in the downward direction along gravity. B denotes the body frame, which co-incides with the IMU frame, and C denotes the camera frame. B_i and C_i denote the body frame and camera frame at time t_i respectively. R_{ji} and t_{ji} , together written as the homogeneous matrix T_{ji} , denote the rotation and translation that transforms points from the frame at t_i to the frame at t_j . The frame can be the camera frame or the body frame, depending on the context. R_i and t_i denote the rotation and translation of the frame at t_i with respect to the world frame. u^l denotes the normalized 2D image coordinates of the l -th visual feature. The corresponding 3D point p_l is represented by its inverse depth λ_l with respect to its first frame of observation. A plane π_p is represented by its normal and distance parameters (\mathbf{n}, d) , with respect to the C_0 frame. The planar homography matrix (Fig. 2) which maps the 2D image coordinates of a planar point from the C_0 frame to the C_j frame is denoted as H_j .

The state of our system at t_i , \mathbf{x}_i , is defined by the IMU position, orientation, velocity, biases, the inverse depth of the 3D features, and the plane parameters, i.e. $\mathbf{x}_i \doteq [R_i, t_i, v_i, b_i, \{\lambda_l\}, \{\pi_p\}]$.

\mathcal{X} denotes the state of all the frames within the sliding window \mathcal{K} which we want to estimate, i.e. $\mathcal{X} \doteq \{\mathbf{x}_i\}_{i \in \mathcal{K}}$.

B. Front-end

Our system takes as input grayscale images, IMU measurements, and plane segmentation masks. These plane segmentation masks are obtained from a CNN-based model which we describe in Sec. III-E. We apply the obtained plane instance segmentation masks on the original images to detect and track only the features that belong to the (static) planar regions in the scene, while also maintaining information about which plane each tracked feature belongs to. To avoid detecting any features along the edges of the mask which might belong to a dynamic object, we apply an erosion operation on the original masks. Further, we use RANSAC to fit a separate planar homography model to the features from each plane to discard any outliers. These outliers could be features arising from incorrect matches by the KLT optical flow algorithm, or from inaccurate segments that do not belong to the larger parent plane. The raw IMU measurements between image frames are converted into preintegrated measurements and image frames with sufficient parallax and feature tracks are selected as keyframes.

C. Initialization

The main visual-inertial sliding-window optimization is non-convex and is minimized iteratively which requires an accurate initial estimate. To obtain a good initial estimate without making any assumptions about the starting configuration, a separate loosely-coupled initialization procedure is used where the visual measurements and inertial measurements are processed separately into their respective pose estimates and then aligned together to solve for the unknowns in multiple steps.

We begin by first solving for the camera poses, the 3D points, and the plane parameters. From a window of initial image frames, two base frames are selected such that they have sufficient parallax between them. Out of all the feature correspondences between them we select the correspondences that arise from the largest plane in the scene. We identify the plane which has the largest number of features as the largest plane. Using these correspondences, we fit a planar homography matrix H relating the two camera poses and the largest plane using RANSAC. This homography matrix is normalized and then decomposed into the rotation, translation, and plane normal using the analytical method of Malis and Vargas [34], as implemented in OpenCV [35]. The method however returns up to four different solution tuples which must be reduced to one. We first reduce this solution set to two by enforcing the positive depth constraint, that is, all the plane features must lie in front of the camera. We implement this as the constraint, $\mathbf{n}_i^T \mathbf{u}_\mu > 0$, where \mathbf{u}_μ is the mean 2D feature point in normalized image coordinates. From the resulting two possible solutions, we finally select the one whose rotation (after transforming to B frame) is closest to the corresponding preintegrated IMU rotation $\Delta \tilde{R}_{ij}$,

$$\arg \min_k \|\Delta \tilde{R}_{ij}^T (R_{BC} R_{ij}^k R_{BC}^T) - I\|^2$$

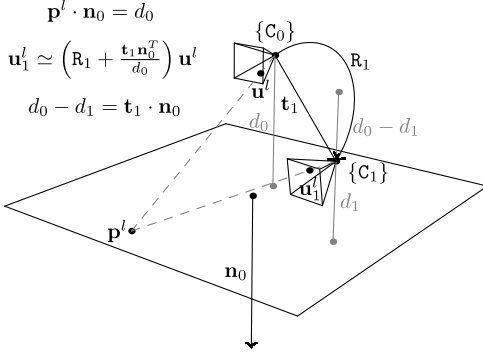


Fig. 2: The planar homography matrix $H_1 = \left(R_1 + \frac{t_1 n_0^T}{d_0} \right)$ is a 3×3 matrix, arising from the planar constraint $p^l \cdot n_0 = d_0$, which maps the observation u^l from the first frame to u_1^l in the second frame. The known ambiguity in its decomposition can be resolved using the IMU.

Even though the gyroscope bias inside the preintegrated IMU rotation is not estimated yet, its magnitude is usually too small to cause a difference in the solution. The estimated pose from the decomposition is then used to triangulate the 3D positions of the feature correspondences between the two base frames and obtain an initial point cloud. The poses of the remaining frames within the window are estimated with respect to this point cloud using PnP. We note here that since the estimated pose between the two base frames is in the scale of the plane distance d , the triangulated point cloud and the deduced poses are also in the same scale. All the pose estimates are then fed into a visual bundle adjustment solver where, in addition to the standard 3D-2D reprojection residual, we include the following 2D-2D reprojection residual arising from the planar homography,

$$r_H = u_j^l - \left(R_j + \frac{t_j n^T}{d} \right) u^l$$

This residual measures the discrepancy between the expected observation of the point p^l in frame C_j , obtained by mapping its corresponding image location u^l from the first frame using the planar homography matrix, and the true observation u_j^l . This is also illustrated in Fig. 2. The output of the bundle adjustment is the up-to-scale (d) camera poses and 3D feature points, and the plane normal.

These bundle adjusted visual estimates are still not sufficient to initialize the optimization, as the unknown scale, gravity vector, velocities, and biases in the IMU also need to be estimated. These quantities are estimated using the same divide-and-conquer approach used in [12]. The solved scale factor between the visual estimates and the preintegrated IMU measurements is the distance to the largest plane d . The accelerometer bias, which typically requires more measurements, is not solved for to limit the initialization time to less than 2 seconds.

Once all the inertial quantities are estimated, the camera poses and 3D feature points are re-scaled to metric units and the world frame is re-aligned such that its Z-axis is

in the direction of gravity. For the planes in the scene other than the largest plane, including planes that might be newly observed during operation, we similarly compute their respective planar homography matrices and decompose them. But we avoid re-doing the visual bundle adjustment and the re-alignment of their poses with the IMU measurements to estimate their scale factors d_p . We instead directly estimate d_p as the inverse ratio of each decomposed translation t_p (which is in the scale of d_p as $\frac{t}{d_p}$) to the corresponding metric translation t , which has already been estimated previously using the largest plane and inertial measurements. With this, all the visual and inertial quantities in our state have been solved for, and these estimates are fed into the sliding-window estimator as the initial seed for the optimization.

D. Sliding-window Optimization

A full batch optimization of the entire history of poses, map points, inertial and plane parameters quickly becomes computationally infeasible for real-time operation. Instead, a sliding-window of a fixed number of frames are optimized over their associated inertial and visual measurements. The optimization objective is described formally as follows.

We denote with \mathcal{I}_{ij} the set of all IMU measurements between two consecutive frame instances i and j within the window \mathcal{K} . The set of all image features observed in frame i is denoted as \mathcal{C}_i , and the set of all observed planes is denoted as \mathcal{P} . A factor graph representation of the states and measurements within a simplified window is shown in Fig. 3. The MAP estimate \mathcal{X}^* of all the states in the sliding window is obtained as the minimum of the sum of the squared residual errors,

$$\begin{aligned} \mathcal{X}^* \doteq \arg \min_{\mathcal{X}} & \|r_p\|^2 + \sum_{(i,j) \in \mathcal{K}} \|r_{\mathcal{I}_{ij}}\|^2 \\ & + \sum_{i \in \mathcal{K}} \sum_{l \in \mathcal{C}_i} \rho(\|r_{\mathcal{C}_{il}}\|^2) + \sum_{p \in \mathcal{P}} \sum_{i \in \mathcal{K}} \sum_{l \in \mathcal{C}_i} \rho(\|r_H\|^2) \end{aligned}$$

where r_p is the prior residual resulting from marginalization of the previous states, $r_{\mathcal{I}_{ij}}$ is the preintegrated IMU residual and $r_{\mathcal{C}_{il}}$ is the standard 3D-2D reprojection residual as defined in [12]. ρ is a Cauchy loss that is used to down-weight any outliers. r_H is our planar homography residual that is defined as,

$$r_H = u_j^l - T_{BC}^{-1} \left(R_{ji} + \frac{t_{ji} n_i^p}{d_i^p} \right) T_{BC} u_i^l$$

This term is similar to the one used in the initialization except the pose and plane parameters are in the body frame. The p -th plane normal n^p and depth d^p which are both originally defined in the first camera frame C_0 are transformed to the current body frame B_i as follows,

$$\begin{aligned} n_{B_i} &= R_i^T R_{BC} n_{C_0} \\ d_{B_0} &= d_{C_0} + t_{BC} \cdot n_{B_0} \\ d_{B_i} &= d_{B_0} - t_{B_0 B_i} \cdot n_{B_0} \end{aligned}$$

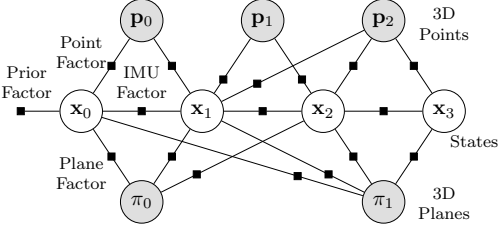


Fig. 3: A factor graph representation of the (simplified) sliding window optimization showing the states and measurements linked together by the IMU, vision, and plane factors.

This entire non-linear objective function is minimized iteratively using the Dogleg algorithm with Dense-Schur linear solver implemented in Ceres Solver [36]. At the end of the optimization, the window is moved forward by one frame to incorporate the latest frame. The state of the latest frame is initialized by propagating the inertial measurements from the previous frame. The dropped frame is marginalized as done in [12]. The optimized plane parameters however are not dropped or marginalized and are instead reused as and when the plane is observed again.

E. Plane Segmentation

To segment the plane instances from each input RGB image, we start with the Plane-Recover [37] model. Their model is trained using a structure-induced loss to simultaneously predict plane segmentation masks and their 3D parameters, with only semantic labels and no explicit 3D annotations. The model runs on a single Nvidia GTX Titan X (Maxwell) GPU at 30 FPS which also makes it suitable for real-time VIO.

Despite the effectiveness of their model, we noticed in our experiments that the predicted segments are often not continuous and single large planes were segmented as multiple separate planes. To overcome this we introduce an additional inter-plane loss function that constrains planes with small relative orientations between them into a single plane.

$$\mathcal{L}_{\text{inter}} = \frac{1}{n} \sum_{i=1}^n \sum_{j=1}^m \|\mathbf{n}_i^j \cdot \mathbf{n}_i^j - l_i\|^2$$

where \mathbf{n} is the plane normal, m is the number of planes which we fix to 3, n is the number of images in a batch, and l_i is the inter-plane label generated online that is assigned the value 1 if $\angle(\mathbf{n}_i^j, \mathbf{n}_i^j) < \frac{\pi}{4}$ and 0 otherwise.

With this added loss function, we retrain the network with their provided training data from SYNTHIA, and we additionally train on two sequences (00, 01) from the indoor ScanNet dataset. To further improve the segmentation and capture the fine boundary details, we employ a fully dense conditional random field (CRF) model [38] that refines the network's segmentations. We use its default parameters as such without much tuning. Segmentation outputs from the model for an unseen real-world sequence that we use in our evaluations are visualized in Fig. 5.

To summarize, in this section we've described how we detect and track planar features from the scene, how we decompose their induced planar homography matrices into their respective motion and plane estimates using the IMU, and how we introduce the plane parameters as added constraints into the initializer and the sliding-window optimization. In the next section we demonstrate the effectiveness of this approach in dynamic environments.

IV. EXPERIMENTS

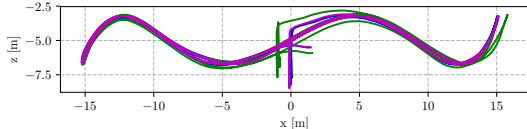
We demonstrate using both simulated data and real-world data that using only planar features and their induced planar homography constraints leads to an improvement in estimation accuracy in dynamic environments. All the evaluations are run on a 6-core Intel Core i5-8400 CPU with 8 GB RAM and a 1 TB HDD. To account for randomness from RANSAC and the multi-tasking OS, we report the median results from five runs for each evaluation. All code and data to reproduce our results are available on our project page.

A. Simulation Experiments

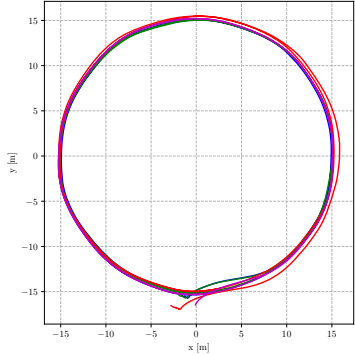
RPVIO-Sim Dataset: For reasons explained in Sec. II-C, we generate our own dataset in simulation with accurate sensors and ground truth trajectories, and with sufficient IMU excitation throughout the sequences. We progressively add dynamic elements to these sequences and keep them visible in all parts of the sequences, even during initialization. This allows us to isolate their effect on the overall system accuracy.

We build a custom indoor warehouse environment with dynamic characters in Unreal Engine [39]. We borrow several high-quality and feature-rich assets from the FlightGoggles [40] project for photorealism. This environment is integrated with AirSim [41] to spawn a quadrotor and collect visual-inertial data. We collect monocular RGB images and their plane instance masks at 20 Hz, IMU measurements and ground truth poses at 1000 Hz. The IMU measurements are sub-sampled to 200 Hz for our experiments. The camera and IMU intrinsics, and the camera-IMU spatial transform are obtained directly from AirSim. A time-offset of 0.03s between the camera and IMU measurements, introduced by the recording process, is calibrated using Kalibr [42].

The quadrotor is controlled to move along a circle of radius 15 m, while moving along a sine wave in the vertical direction, resulting in a sinusoidal pattern. The sine excitation along the height is to ensure a non-constant acceleration and keep the scale observable [4]. We further command it to accelerate vertically at the beginning of its motion, before following the trajectory, to help the initialization. The total trajectory is of 200 m length and 80 s duration, with a maximum speed of 3 m/s. Within the circle formed by the quadrotor, we introduce dynamic characters that are performing a repetitive dance motion. We progressively add more dynamic characters to each sequence, keeping everything else fixed, starting from no characters (static) and going up to 8 characters (C8), recording six sequences in total. The yaw-direction of the quadrotor is also fixed to



(a) Side-view comparison between VINS-Mono (green), RP-VIO-Single (blue), and ground truth (magenta) on the C2 sequence. VINS-Mono accumulates error during its initialization (vertical motion), while RP-VIO-Single tracks accurately throughout the sequence.



(b) Top-view comparison between Mask-VINS (red), RP-VIO-Single (blue), RP-VIO-Multi (green), and ground truth (magenta) on the C6 sequence. Original VINS-Mono fails to track completely and is not included. Both RP-VIO-Single and RP-VIO-Multi are closer to the ground truth than Mask-VINS.

Fig. 4: Trajectory comparisons from our simulated experiments.

keep the camera pointing towards the center of the circle, such that the characters are in the field-of-view of the camera for the entire sequence. The quadrotor and the characters are controlled programmatically to ensure their motions are also in sync across all the sequences.

Evaluation: We evaluate VINS-Mono [12], and our proposed method on these generated sequences. We use two versions of our method, RP-VIO-Single and RP-VIO-Multi. RP-VIO-Single includes in the optimization only features from the largest plane visible at any time, while RP-VIO-Multi includes features from all the visible planes. We also create another version of VINS-Mono, called Mask-VINS, that is modified to take as an additional input the same plane instance masks as ours. It uses these masks to detect and track all the features that belong to all the static planar regions in the environment while avoiding features from all the dynamic characters, similar to [10]. It uses the same feature parameters as ours, and the masks are also eroded to avoid tracking features along the mask edges which might belong to dynamic characters. The back-end remains the same as VINS-Mono. We use this additional version to investigate the effect of the added planar homography residual term r_H in the optimization. We compute the RMSE of the estimated trajectories of each method for every sequence, after SE(3) alignment [43] with the ground truth trajectories, and report them in Tab. I.

Discussion: The performance of VINS-Mono, Mask-VINS, and RP-VIO on the static and one character sequences are very similar. Since the number of static points are much greater than the number of dynamic points, the effect of RANSAC is the same as applying the mask. In the two

TABLE I: Results of the evaluation on our generated dataset. We report the median RMSE from five runs on each sequence. X denotes complete tracking failure. Results which show a significant improvement are underlined.

Seq.	Absolute Trajectory RMSE (m)			
	VINS-Mono	Mask-VINS	RP-VIO-Multi	RP-VIO-Single
Static	0.21	-	0.19	0.19
C1	0.24	0.23	0.28	0.23
C2	0.85	0.21	0.24	0.18
C4	X	0.68	0.76	0.56
C6	X	0.91	0.62	0.54
C8	X	X	0.77	0.85

character sequence we note that VINS-Mono has a much lower accuracy than Mask-VINS and RP-VIO, while the accuracy of Mask-VINS and RP-VIO are again similar. VINS-Mono accumulates most of the error during the initialization as shown in 4a, when one of the characters is close to the camera. In the four, six, and eight character sequences however VINS-Mono’s initialization error is too high and it loses track completely. Mask-VINS and RP-VIO are still able to track successfully in C4 and C6, but RP-VIO-Single is the most accurate (also shown in Fig. 4b) which alludes to the role of the added homography constraints in the improved robustness. In the C8 sequence ours is still able to track successfully like the other sequences but Mask-VINS loses track completely. This could be because the scene is very cluttered and the few features that are left come only from a single plane during initialization which is a degenerate case for VINS-Mono’s fundamental matrix based SfM initializer. RP-VIO-Multi shows a better accuracy than RP-VIO-Single in this sequence which could be because unlike in the previous sequences RP-VIO-Single has fewer stable features to track than RP-VIO-Multi.

B. Experiments on Standard Datasets

Sequences: We evaluate the robustness of our system on three more sequences from three diverse datasets. The first sequence is from the newly released VIODE [10] dataset, that was also generated using AirSim. This sequence was captured in an outdoor city environment with many moving vehicles, from a drone that is performing very aggressive maneuvers including sharp rotations. We use their provided segmentation images to track features only along the road. The second sequence is from the OpenLORIS-Scene [13] dataset. This was captured in a real-world supermarket from a floor-cleaning robot that contains many dynamic characters in the form of moving people, trolleys, and bags. The third sequence is from the ADVIO [14] dataset that was captured from a hand-held smartphone in a real-world metro station. This is the most visually challenging sequence out of the three, with a narrow field-of-view and fast motions, and dynamic characters in the form of a large moving train and moving people. The total length of the VIODE sequence is 166 m, the OpenLORIS sequence is 145 m, and the ADVIO



Fig. 5: Segmentation outputs for two challenging images in the OpenLORIS sequence, from the original model and the model modified with our inter-plane loss are visualized. The output from our model is further refined with a dense-CRF, before being used by our VIO system, and is also visualized here.

sequence is 136 m.

Evaluation: We use the single-plane version of our method for all the three sequences since they contain predominantly only a single large plane that can be tracked reliably at a time. We use the same feature parameters that were used for the simulation experiments without any tuning. We compute the RMSE ATE of its estimated trajectories with respect to the ground truth after $SE(3)$ alignment and compare against VINS-Mono. The median errors from five runs for each sequence are reported in Tab. II. Since all the masked features predominantly come from a single plane in all the three sequences, we do not compare against Mask-VINS that was used in the earlier evaluation since features from a single plane form a degenerate configuration for the VINS-Mono initializer. The unavailability of an off-the-shelf semantic classifier that can accurately segment all the dynamic objects present in both the sequences also makes a fair comparison not possible. The images in the ADVIO sequence are of a very high resolution 1280×720 and come at a high rate of 60 Hz which causes a lot of frame drops in the VINS front-end. For this reason the evaluation on this sequence alone is run on a more powerful Intel Xeon CPU with 32GB RAM and an SSD.

TABLE II: Results of the evaluations on three diverse sequences. We report the median RMSE from five runs on each sequence.

Sequence	Absolute Trajectory RMSE (m)	
	VINS-Mono	RP-VIO-Single
VIODE-city-night-high	0.73	0.32
OpenLORIS-market-1	2.45	1.35
ADVIO-12	4.34	2.75

Discussion: Our method shows a significant improvement over VINS-Mono on all three sequences. In the OpenLORIS and VIODE sequences, our method used a lesser number of features than VINS-Mono despite which it has shown greater accuracy. This makes us believe that it might be sufficient to track few stable features than tracking all possible features, of which many can be noisy. On both the real-world sequences, despite using a generic plane detection network that has not been trained on their images, the network and the CRF are

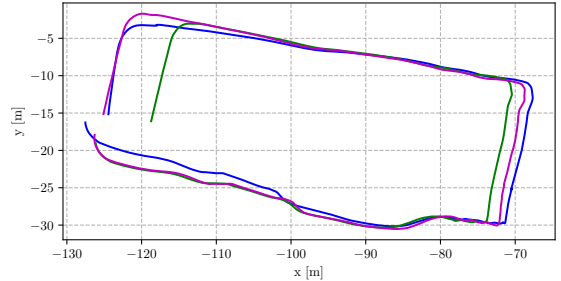


Fig. 6: Top-view comparison between RP-VIO-Single (blue), VINS-Mono (green), and ground truth (magenta), on the OpenLORIS market-1 sequence.

able to provide reliable plane segmentations that are good enough for our method to track accurately. If training data is available, we expect more accurate segmentations and a better overall trajectory estimate. For scenes which contain dynamic planar surfaces such as vehicles, specific ground or wall surface classifiers must be trained and used instead. Training for specific planar surfaces is still more feasible than training semantic classifiers for all possibly moving object classes. In the absence of clear planar structures however, our method should be considered complimentary to general-purpose point-based systems as and when planes become visible, and not as a complete replacement.

V. CONCLUSION

We have proposed a monocular VIO system that uses only one or more planes in the environment and their structural regularity for an accurate motion estimation in dynamic environments. We have validated its improved performance in diverse simulated and real-world dynamic environments, while showing the same baseline performance in static environments. For real-world environments, using only a generic plane segmentation model, we showed an improvement of up to 45% over a state-of-the-art monocular VIO system. We have also shown in our comparison with Mask-VINS in simulation that our approach achieves better accuracy than a simple dynamic-features masking approach which alludes to the role of the added structural constraints in the improved robustness. The future scope of this work is to extend it into a

full SLAM system to obtain clean and consistent plane-based maps, without any off-the-plane noisy features, that can in turn be used to improve the motion estimates further. Further, it can be investigated if the predicted 3D plane parameters from the segmentation model can be used directly for an improved initialization. The approach can also be extended to incorporate corresponding line features that arise from the segmented planes.

REFERENCES

- [1] H. Oleynikova, C. Lanegger *et al.*, “An open-source system for vision-based micro-aerial vehicle mapping, planning, and flight in cluttered environments,” *Journal of Field Robotics*, vol. 37, no. 4, pp. 642–666, 2020.
- [2] Facebook, “Oculus vr.” <https://oculus.com>.
- [3] Microsoft, “Hololens,” <https://microsoft.com/en-us/hololens>.
- [4] K. J. Wu, C. X. Guo, G. Georgiou, and S. I. Roumeliotis, “VINS on wheels,” in *2017 IEEE International Conference on Robotics and Automation (ICRA)*, May 2017, pp. 5155–5162.
- [5] Y. Yang, P. Geneva, K. Eckenhoff, and G. Huang, “Degenerate motion analysis for aided ins with online spatial and temporal sensor calibration,” *IEEE Robotics and Automation Letters*, vol. 4, no. 2, pp. 2070–2077, 2019.
- [6] Y. Yang, P. Geneva, X. Zuo, and G. Huang, “Online IMU intrinsic calibration: Is it necessary?” in *Robotics: Science and Systems XVI*. Robotics: Science and Systems Foundation, Jul. 2020.
- [7] R. I. Hartley and A. Zisserman, *Multiple View Geometry in Computer Vision*, 2nd ed. Cambridge University Press, ISBN: 0521540518, 2004.
- [8] A. Kundu, K. M. Krishna, and J. Sivaswamy, “Moving object detection by multi-view geometric techniques from a single camera mounted robot,” in *2009 IEEE/RSJ International Conference on Intelligent Robots and Systems*. IEEE, 2009, pp. 4306–4312.
- [9] J. Vertens, A. Valada, and W. Burgard, “SMSnet: Semantic motion segmentation using deep convolutional neural networks,” in *2017 IEEE/RSJ International Conference on Intelligent Robots and Systems (IROS)*, Sep. 2017, pp. 582–589.
- [10] K. Minoda, F. Schilling *et al.*, “Viode: A simulated dataset to address the challenges of visual-inertial odometry in dynamic environments,” *IEEE Robotics and Automation Letters*, pp. 1–1, 2021.
- [11] C. Yu, Z. Liu *et al.*, “DS-SLAM: A semantic visual SLAM towards dynamic environments,” in *2018 IEEE/RSJ International Conference on Intelligent Robots and Systems (IROS)*, Oct. 2018, pp. 1168–1174.
- [12] T. Qin, P. Li, and S. Shen, “VINS-Mono: A robust and versatile monocular Visual-Inertial state estimator,” *IEEE Trans. Rob.*, vol. 34, no. 4, pp. 1004–1020, Aug. 2018.
- [13] X. Shi, D. Li *et al.*, “Are we ready for service robots? the OpenLORIS-Scene datasets for lifelong SLAM,” in *2020 International Conference on Robotics and Automation (ICRA)*, 2020, pp. 3139–3145.
- [14] S. Cortés, A. Solin, E. Rahtu, and J. Kannala, “ADVIO: An authentic dataset for visual-inertial odometry,” in *Proceedings of the European Conference on Computer Vision (ECCV)*, 2018, pp. 419–434.
- [15] G. Huang, “Visual-inertial navigation: A concise review,” in *2019 international conference on robotics and automation (ICRA)*. IEEE, 2019, pp. 9572–9582.
- [16] C. Campos, R. Elvira *et al.*, “ORB-SLAM3: An accurate open-source library for visual, visual-inertial and multi-map SLAM,” *arXiv preprint arXiv:2007.11898*, 2020.
- [17] A. Rosinol, M. Abate, Y. Chang, and L. Carlone, “Kimera: an open-source library for real-time metric-semantic localization and mapping,” in *IEEE Intl. Conf. on Robotics and Automation (ICRA)*, 2020. [Online]. Available: <https://github.com/MIT-SPARK/Kimera>
- [18] A. I. Mourikis and S. I. Roumeliotis, “A multi-state constraint kalman filter for vision-aided inertial navigation,” in *Proceedings 2007 IEEE International Conference on Robotics and Automation*. IEEE, 2007, pp. 3565–3572.
- [19] P. Geneva, K. Eckenhoff *et al.*, “Openvins: A research platform for visual-inertial estimation,” in *Proc. of the IEEE International Conference on Robotics and Automation*, Paris, France, 2020.
- [20] V. Indelman, S. Williams, M. Kaess, and F. Dellaert, “Factor graph based incremental smoothing in inertial navigation systems,” in *2012 15th International Conference on Information Fusion*. IEEE, 2012, pp. 2154–2161.
- [21] M. Hsiao, E. Westman, and M. Kaess, “Dense planar-inertial slam with structural constraints,” in *2018 IEEE International Conference on Robotics and Automation (ICRA)*. IEEE, 2018, pp. 6521–6528.
- [22] S. Leutenegger, S. Lynen *et al.*, “Keyframe-based visual-inertial odometry using nonlinear optimization,” *The International Journal of Robotics Research*, vol. 34, no. 3, pp. 314–334, 2015.
- [23] C. Forster, L. Carlone, F. Dellaert, and D. Scaramuzza, “On-Manifold preintegration for Real-Time Visual-Inertial odometry,” *IEEE Trans. Rob.*, vol. 33, no. 1, pp. 1–21, Feb. 2017.
- [24] A. Rosinol, T. Sattler, M. Pollefeys, and L. Carlone, “Incremental visual-inertial 3d mesh generation with structural regularities,” in *2019 International Conference on Robotics and Automation (ICRA)*. IEEE, 2019, pp. 8220–8226.
- [25] Y. Yang, P. Geneva *et al.*, “Tightly-coupled aided inertial navigation with point and plane features,” in *2019 International Conference on Robotics and Automation (ICRA)*, 2019, pp. 6094–6100.
- [26] G. Panahandeh, S. Hutchinson, P. Händel, and M. Jansson, “Planar-Based visual inertial navigation: Observability analysis and motion estimation,” *J. Intell. Rob. Syst.*, vol. 82, no. 2, pp. 277–299, May 2016.
- [27] B. Fu, K. S. Shankar, and N. Michael, “Rad-vio: Rangefinder-aided downward visual-inertial odometry,” in *2019 International Conference on Robotics and Automation (ICRA)*, 2019, pp. 1841–1847.
- [28] X. Li, Y. Li *et al.*, “Co-planar parametrization for stereo-slam and visual-inertial odometry,” *IEEE Robotics and Automation Letters*, vol. 5, no. 4, pp. 6972–6979, 2020.
- [29] M. R. U. Saputra, A. Markham, and N. Trigoni, “Visual SLAM and structure from motion in dynamic environments: A survey,” *ACM Comput. Surv.*, vol. 51, no. 2, pp. 1–36, Feb. 2018.
- [30] K. Eckenhoff, Y. Yang, P. Geneva, and G. Huang, “Tightly-Coupled Visual-Inertial localization and 3-D Rigid-Body target tracking,” *IEEE Robotics and Automation Letters*, vol. 4, no. 2, pp. 1541–1548, Apr. 2019.
- [31] M. Shan, Q. Feng, and N. Atanasov, “Orcvio: Object residual constrained visual-inertial odometry,” in *2020 IEEE/RSJ International Conference on Intelligent Robots and Systems (IROS)*, 2020, pp. 5104–5111.
- [32] B. P. W. Babu, D. Cyganski, J. Duckworth, and S. Kim, “Detection and resolution of motion conflict in visual inertial odometry,” in *2018 IEEE International Conference on Robotics and Automation (ICRA)*, May 2018, pp. 996–1002.
- [33] M. Bloesch, M. Burri *et al.*, “Iterated extended kalman filter based visual-inertial odometry using direct photometric feedback,” *The International Journal of Robotics Research*, vol. 36, no. 10, pp. 1053–1072, 2017.
- [34] E. Malis and M. Vargas, “Deeper understanding of the homography decomposition for vision-based control,” INRIA, Tech. Rep. inria-00174036, 2007.
- [35] G. Bradski, “The OpenCV Library,” *Dr. Dobb’s Journal of Software Tools*, 2000.
- [36] S. Agarwal, K. Mierle, and Others, “Ceres solver,” <https://ceres-solver.org>.
- [37] F. Yang and Z. Zhou, “Recovering 3d planes from a single image via convolutional neural networks,” in *Proceedings of the European Conference on Computer Vision (ECCV)*, 2018, pp. 85–100.
- [38] P. Krähenbühl and V. Koltun, “Efficient inference in fully connected crfs with gaussian edge potentials,” *arXiv preprint arXiv:1210.5644*, 2012.
- [39] E. Games, “Unreal engine,” <http://unrealengine.com>.
- [40] W. Guerra, E. Tal *et al.*, “FlightGoggles: Photorealistic sensor simulation for perception-driven robotics using photogrammetry and virtual reality,” in *2019 IEEE/RSJ International Conference on Intelligent Robots and Systems (IROS)*. IEEE, Nov. 2019, pp. 6941–6948.
- [41] S. Shah, D. Dey, C. Lovett, and A. Kapoor, “AirSim: High-Fidelity visual and physical simulation for autonomous vehicles,” in *Field and Service Robotics*. Springer International Publishing, 2018, pp. 621–635.
- [42] P. Furgale, J. Rehder, and R. Siegwart, “Unified temporal and spatial calibration for multi-sensor systems,” in *2013 IEEE/RSJ International Conference on Intelligent Robots and Systems*, Nov. 2013, pp. 1280–1286.
- [43] Z. Zhang and D. Scaramuzza, “A tutorial on quantitative trajectory evaluation for Visual-(Inertial) odometry,” in *2018 IEEE/RSJ International Conference on Intelligent Robots and Systems (IROS)*, Oct. 2018, pp. 7244–7251.